An Adaptive Switching Frequency and Conduction Loss Optimization Modulation Strategy for Single-Phase Soft-Switching Inverter

Chaofan Wei, Jianhua Lei, Ruogu Yao, Jiatao Yang, Rui Li, *Senior Member, IEEE*, Wei Yu, and Shaohui Li

***Abstract*—Single-phase full-bridge inverter operating in triangular current mode (TCM) can realize zero-voltage switching to achieve high efficiency. However, the TCM full-bridge inverter features a wide range of switching frequency variation, especially near the ac current zero-crossing point (ZCP), which increases the switching loss and control difficulty. In this article, an adaptive optimal quasi-trapezoidal current mode (QTCM) control strategy is proposed based on the output characteristics of the full-bridge inverter, which reduces the switching frequency and inductor current rms by adjusting the durations of the different operating modes. The relationship between the zero level ratio *m* of the inverter output and the switching frequency and the peak inductor current is established. By adjusting the ratio *m*, co-optimization of switching frequency and conduction loss is implemented according to the output voltage and current. The switching sequence of the power switches is improved to achieve the seamless switching of the ac current ZCP. A 1-kW prototype with Gallium nitride (GaN) devices is built to verify the effectiveness of proposed modulation strategy with a peak efficiency of 98.3%. Compared with TCM, the proposed QTCM has a higher efficiency over the whole load range with the same hardware cost.**

***Index Terms*—Co-optimization, quasi-trapezoidal current mode (QTCM), triangular current mode (TCM), zero-voltage switching (ZVS).**

I. INTRODUCTION

SINGLE-PHASE inverters are widely used in photovoltaic power generation, vehicle transportation, uninterruptible power supply, and other fields. In small and medium power applications, the use of wide-bandwidth devices, such as Gallium nitride (GaN) HFETs, can significantly increase the switching frequency and reduce the size of passive components to increase the power density of the converter [1], [2]. However, high switching frequency also brings additional switching loss. For enhanced GaN HFETs, their almost zero reverse recovery charge characteristics result in small turn-OFF loss, and the turn-ON loss due to the junction capacitance is much larger than the turn-OFF loss [3], [4]. Zero-voltage switching (ZVS) technique is usually used to reduce the switching loss [5].

To realize soft switching of the inverter, there are the following two schemes: 1) increasing the auxiliary resonant network and 2) increasing the inductor current ripple during the switching cycle so that the current direction meets the ZVS requirements. A soft-switching inverter topology with the addition of a resonant branch in the dc link is proposed in [6] and [7], which transfers the dc bus voltage to the resonant branch to realize ZVS. An *LC* series resonant loop is added between the dc bus and the ac output to transfer the inductor current ripple to the capacitor to provide the energy required for ZVS [8]. Liu et al. [9] added an active auxiliary branch on the ac output side to realize ZVS for the main power devices and zero-current switching (ZCS) for the auxiliary switches. However, soft-switching techniques based on auxiliary resonant networks make the circuit structure more complex and the additional component requirements reduce the power density of the system.

In order to realize soft switching without adding additional devices, a triangular current mode (TCM) or boundary current mode (BCM) modulation strategy is proposed in [10] and [11], which satisfies the ZVS condition by operating at variable switching frequency so that the inductor current is reversed during the switching cycle. The simplicity of TCM implementation has attracted the interest of many researchers and has been optimized in different directions. The loss distribution of micro inverters with fixed reverse current, variable reverse current, and constant bandwidth current is compared [12], [13]. Based on the comparison results, a dual-mode current modulation strategy combining ZVS and ZCS is proposed to improve the efficiency. A hybrid modulation strategy with constant peak current is proposed in [14], where BCM is used to reduce the current rms at high power output and discontinuous conduction mode (DCM) is used to reduce the switching frequency at low power output. For the symmetrical dual synchronous Buck inverter, an average current control mode with variable PWM frequency is proposed without high-speed current sampling [15].

Received 27 June 2025; revised 5 August 2025; accepted 5 September 2025. Date of publication 12 September 2025; date of current version 23 December 2025. This work was supported in part by the Dongguan Key Research and Development Project under Grant 20221200300022 and in part by the National Natural Science Foundation of China under Grant 52577208. Recommended for publication by Associate Editor H. H.-C. Iu. *(Corresponding author: Rui Li.)*

Chaofan Wei, Ruogu Yao, Jiatao Yang, and Rui Li are with the Key Laboratory of Control of Power Transmission and Conversion, School of Electronics, Information, and Electrical Engineering, Shanghai Jiao Tong University, Shanghai 200240, China (e-mail: weichaofan@sjtu.edu.cn; ruogu_yao@sjtu.edu.cn; yangjiatao@sjtu.edu.cn; liruiqd@sjtu.edu.cn).

Jianhua Lei is with Shenzhen Poweroak Newener Company, Ltd., Shenzhen 518000, China (e-mail: leijh@poweroak.net).

Wei Yu and Shaohui Li are with East Group Company, Ltd., Dongguan 523808, China (e-mail: yuw@eastups.com; lish@eastups.com).

Color versions of one or more figures in this article are available at https://doi.org/10.1109/TPEL.2025.3609768.

Digital Object Identifier 10.1109/TPEL.2025.3609768

TCM modulation can be further categorized into unipolar mode and bipolar mode. Unipolar mode suffers from zero-crossing distortion during zero-voltage crossing area, especially in the case of reactive power output [16]. For bipolar mode, when the inductance of the high-frequency inductor is reduced to tens of μH, the switching frequency near the ac current zero-crossing point (ZCP) will be as high as several MHz [17], [18]. High switching frequency brings greater challenges to digital control systems, sampling, and protection [19]. Switching loss, core loss, and other losses related to switching frequency also increase significantly [20]. In addition, when switching frequency reaches MHz, the effect of parasitic inductance on the switching process becomes more significant, and the circuit parameter design and layout of the converter will become harsher.

To limit the switching frequency under TCM modulation, researchers have conducted many studies from both topology and control aspects. The constant frequency control of boost PFC is realized by changing the inductance in real time [21], but the design and implementation is complicated. Based on a single-phase inverter with two bridge legs connected in parallel, a hybrid quadrilateral and continuous current mode (HQCCM) with constant frequency is designed, in which ZVS is realized by controlling the phase-shift angle between the two bridge legs of the same phase to generate differential mode currents in the opposite direction [22], [23]. In addition, when BCM modulation is applied in a single-phase multilevel inverter, the voltage difference across the inductor can be reduced by adjusting the output mode. So its switching frequency variation range is smaller than that of a single-phase full-bridge inverter [24], [25].

DCM modulation is a simple and effective way to limit the switching frequency, of which switching frequency can be flexibly adjusted by increasing the turn-OFF time [26], [27]. The DCM can realize ZCS easily, but realizing ZVS requires an accurate implementation of the turn-ON moments during dead time. Besides, operating in DCM will lead to high peak currents. A modulation strategy combining quadrature current and TCM is proposed to solve the current distortion problem during zero-voltage crossing area [16]. However, it is difficult to ensure the ZVS under a wide load range and easy to cause current spikes during mode switching. The switching frequency is effectively reduced by increasing the value of the reverse current [28], [29], [30]. Variable reverse current control is adopted near the ac current ZCP to limit the switching frequency to 1 MHz [28], [29], whereas constant reverse current variable frequency control is used in [30]. Furthermore, a hybrid TCM modulation strategy is proposed based on the loss distribution of TCM and quasi-constant frequency triangle current mode (QCFTCM) [20], which improves the system efficiency by optimizing the ratio of QCFTCM under different loads offline. However, either way of increasing the reverse current brings additional conduction loss as well as core loss. In addition, increasing the reverse current leads to an increase in the peak current, which increases the total turn-OFF current during the switching cycle.

In summary, the switching frequency of TCM can be reduced by increasing the inductor current variation during the switching cycle or decreasing the slope of the inductor current for single-phase full-bridge inverter without changing the topology. This article makes full use of the different operating modes of the inverter and based on this an adaptive optimal quasi-trapezoidal current mode (QTCM) modulation strategy is proposed, which adjusts the durations of the different operating modes according to the output voltage and current. Compared with the previous modulation strategies, the proposed strategy not only effectively reduces the switching frequency but also reduces the switching cycle peak current and inductor current rms.

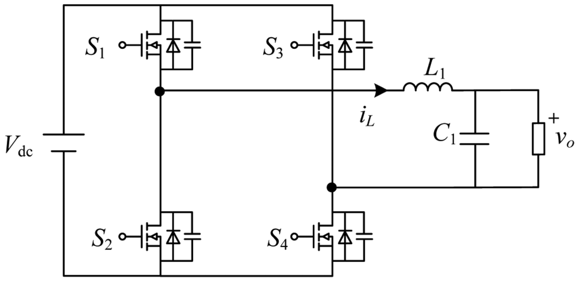

Fig. 1. Topology of single-phase full-bridge inverter.

The rest of this article is organized as follows. In Section II, the principle of QTCM modulation and soft-switching constraints are analyzed, and expressions for key variables such as switching frequency and peak inductor current are derived. In Section III, a power loss model is established and the co-optimization strategy of inductor current rms and switching frequency is proposed. The corresponding closed-loop control strategy and seamless switching method of the ac current ZCP are proposed in Section IV. Experimental results are provided to evaluate the performance of the proposed switching modulation strategies in Section V. Finally, Section VI concludes this article.

II. OPERATING PRINCIPLE OF QTCM SINGLE-PHASE INVERTER

A. Basic Operating Principle of QTCM Modulation

The topology of the single-phase full-bridge inverter is shown in Fig. 1. $V_{\rm dc}$ indicates the dc bus voltage and $i_{\rm L}$ is the inductor current. $v_{\rm o}$ and $i_{\rm o}$ are the output voltage and current of the ac side, respectively. S_1–S_4 are the power switches of the inverter. L_1 and C_1 represent the filter inductor and filter capacitor. The positive direction of the inductor current is shown in Fig. 1. To achieve ZVS for $S_{\rm i}$ ($i = 1$–4), the direction of the inductor current before conduction of $S_{\rm i}$ needs to be the same as the conduction direction of its antiparallel diode, so that the output capacitor of $S_{\rm i}$ is discharged. For S_1 and S_4, $i_{\rm L}$ needs to be negative before conduction, while for S_2 and S_3 $i_{\rm L}$ needs to be positive. The ZVS condition can be satisfied by controlling the inductor current waveform during each switching cycle, as shown in Fig. 2.

In Fig. 2, $i_{\max}$ and $i_{\min}$ denote the upper and lower boundaries of the inductor current envelope, respectively. $i_{\rm oref}$ is the reference value of the output current. To ensure the quality of the output current, the average value of the inductor current $i_{\rm av}$ in each switching cycle should be equal to the reference value of

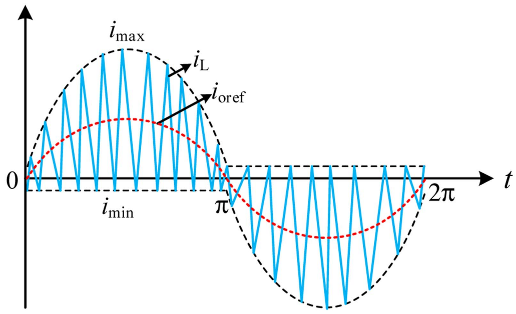

Fig. 2. Diagram of triangle current mode.

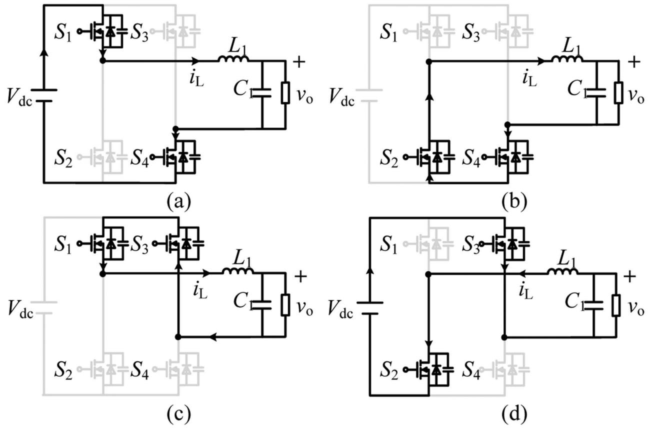

Fig. 3. Single-phase inverter steady state mode of operation. (a) Inverter output positive level. (b), (c) Inverter output zero level. (d) Inverter output negative level.

the output current. $i_{\max}$ and $i_{\min}$ can be calculated as follows:

$$i_{\max} = \begin{cases} 2i_{\text{oref}} + I_a & \sin(\omega t + \varphi) \geq 0 \\ -I_a & \sin(\omega t + \varphi) < 0 \end{cases}$$

$$i_{\min} = \begin{cases} I_a & \sin(\omega t + \varphi) \geq 0 \\ 2i_{\text{oref}} - I_a & \sin(\omega t + \varphi) < 0 \end{cases}$$

$$i_{\text{av}} = \frac{i_{\max} + i_{\min}}{2} = i_{\text{oref}} = I_m \sin(\omega t + \varphi) \qquad (1)$$

where I_m denotes the amplitude of the output current and φ denotes the power factor angle. I_a indicates the value of reverse current.

The single-phase full-bridge inverter can output three levels of V_{dc}, 0, and -V_{dc}, as shown in Fig. 3. In conventional TCM modulation, each switching cycle contains only two levels. Taking the output voltage $v_o > 0$ ($v_o = V_m \sin\omega t$) as an example, S_1 and S_2 operate at high frequency, and S_3 and S_4 operate at line frequency when unipolar modulation is adopted. The inverter output two levels of V_{dc} and 0, corresponding to Fig. 3(a) and (b). The switching frequency f_{su} for the high frequency switches is given as follows:

$$f_{su} = \frac{(V_{dc} - |v_o|)\,|v_o|}{L_1 V_{dc}\,(2\,|i_{\text{oref}}| + 2I_a)}. \qquad (2)$$

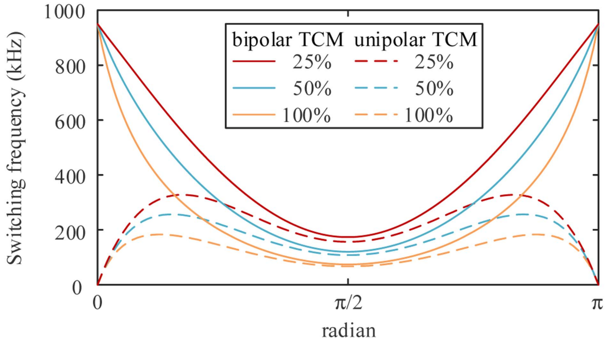

Fig. 4. Switching frequency curves of unipolar TCM and bipolar TCM.

In bipolar modulation, S_1 and S_4 conduct simultaneously. S_2 and S_3 conduct simultaneously. The inverter output two levels of V_{dc} and -V_{dc}, corresponding to Fig. 3(a) and (d). The switching frequency f_{sb} is given as

$$f_{sb} = \frac{V_{dc}^2 - v_o^2}{2L_1 V_{dc}\,(2\,|i_{\text{oref}}| + 2I_a)}. \qquad (3)$$

According to (2) and (3), switching frequency curves of unipolar TCM and bipolar TCM under different operating conditions are plotted, as shown in Fig. 4. The curves in Fig. 4 correspond to the following conditions, $V_{dc} = 380$ V, $V_m = 311$ V, $I_m = 6.428$ A, $I_a = 2$ A, $L_1 = 50$ μH, $\varphi = 0$. According to Fig. 4, the switching frequency of unipolar TCM is close to zero near the ac current ZCP, which is easy to cause output current distortion. In contrast, the switching frequency of bipolar TCM is close to MHz, which results in more switching loss and higher drive requirements. Besides, the overall switching frequency increases as the load is lightened, resulting in a significant drop in efficiency.

Combined with Fig. 3, it can be seen that the reason for such a large difference in the switching frequency between the two modulation methods near the ZCP area is due to the different voltage across the inductor during the inductor current drop stage which causes different slopes of inductor current. The quasi-trapezoidal current mode (QTCM) can be constructed by combining the two modulation methods and making full use of the three levels of the inverter output, as shown in Fig. 5. An additional degree for controlling the range of switching frequency is created in QTCM. Taking Fig. 5(a) as an example, one switching cycle of the proposed QTCM is divided into six intervals shown as Fig. 6.

Interval I [t_0-t_1]: As shown in Fig. 6(a), S_1 and S_4 are ZVS turned ON at t_0. The voltage across the inductor is V_{dc}-v_o and i_L is increased linearly during Interval I.

Interval II [t_1-t_2]: S_1 is turned OFF at t_1 when i_L reaches $i_{\max}$. The output capacitor of S_1 is charged and the output capacitor of S_2 is discharged. When the DS voltage of S_2 decreases to 0, i_L flows through the body diode of S_2 and the ZVS condition is satisfied.

Interval III [t_2-t_3]: S_2 is ZVS turned ON at t_2. The voltage across the inductor is -v_o and i_L is decreased linearly.

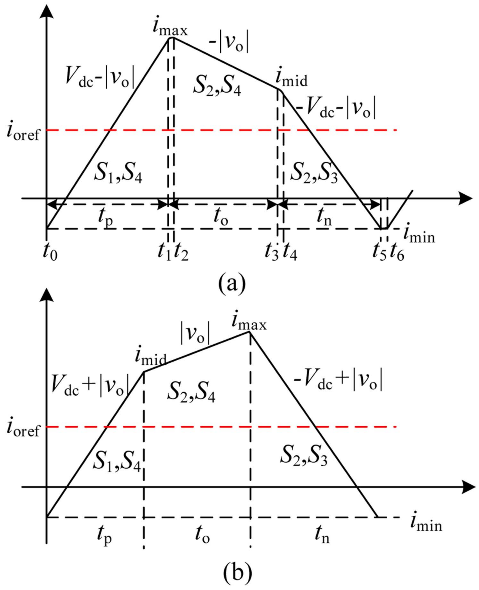

Fig. 5. Diagram of proposed quasi-trapezoidal current mode. (a) $v_o \geqslant 0$, $i_{oref} > 0$. (b) $v_o < 0$, $i_{oref} > 0$.

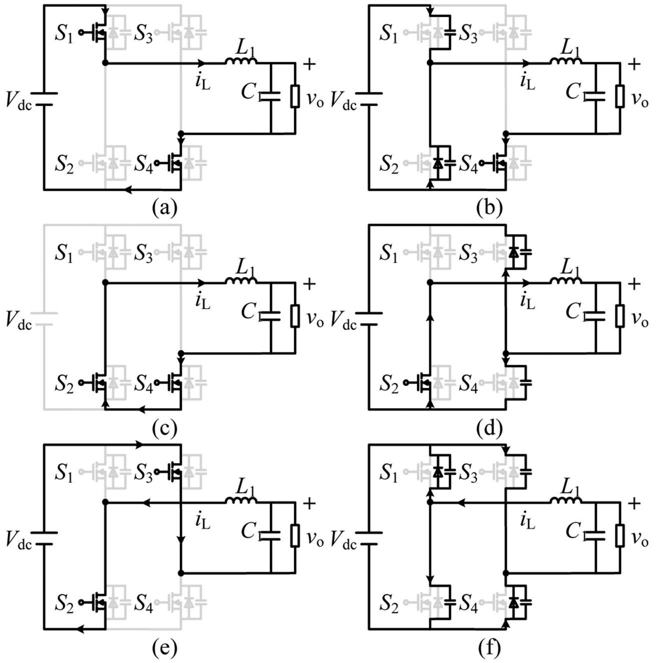

Fig. 6. Operation stages for quasi-trapezoidal current mode. (a) Interval I $[t_0–t_1]$. (b) Interval II $[t_1–t_2]$. (c) Interval III $[t_2–t_3]$. (d) Interval IV $[t_3–t_4]$. (e) Interval V $[t_4–t_5]$. (f) Interval VI $[t_5–t_6]$.

Interval IV $[t_3\text{-}t_4]$: As shown in Fig. 6(d), S_4 is turned OFF at t_3 when i_L reaches i_{mid}. The output capacitor of S_4 is charged and the output capacitor of S_3 is discharged. When the DS voltage of S_3 decreases to 0 during the dead time, i_L flows through the body diode of S_3.

Interval V $[t_4\text{-}t_5]$: S_3 is ZVS turned ON at t_4. The voltage across the inductor is -V_{dc}-v_o and i_L is decreased linearly. i_L is decreased from positive to negative during Interval V.

Interval VI $[t_5\text{-}t_6]$: S_2 and S_3 are turned OFF at t_5 when i_L reaches i_{min}, as shown in Fig. 6(f). The output capacitors of S_2 and S_3 are charged and the output capacitors of S_1 and S_4 are discharged. When the DS voltages of S_1 and S_4 decrease to 0 during the dead time, i_L flows through the body diodes of S_1 and S_4. S_1 and S_4 can realize ZVS. The subsequent process returns to Interval I and repeats.

B. Switching Frequency Characteristics Analysis

In Fig. 5(a), t_p corresponds to the S_1 and S_4 conduction stage of Fig. 3(a), t_o corresponds to the S_2 and S_4 conduction stage of Fig. 3(b), and t_n corresponds to the S_2 and S_3 conduction stages of Fig. 3(c). The conduction intervals and switching period T_s can be calculated as follows:

$$t_p = (i_{max} - i_{min})\, L_1 / (V_{dc} - v_o)$$

$$t_o = (i_{mid} - i_{max})\, L_1 / (-v_o)$$

$$t_n = (i_{min} - i_{mid})\, L_1 / (-V_{dc} - v_o)$$

$$T_s = t_p + t_o + t_n = 1/f_{stp} \tag{4}$$

where f_{stp} represents the switching frequency of QTCM. Defining $t_o = m{*}t_p$, the following expression is yielded according to the principle of inductor volt-second balance:

$$t_p (V_{dc} - v_o) + m t_p (-v_o) + t_n (-V_{dc} - v_o) = 0. \tag{5}$$

The average value of the quasi-trapezoidal current i_{av} is equal to the reference value of the output current i_{oref}

$$\begin{aligned} i_{av} T_s = {} & t_p (i_{max} + i_{min})/2 + t_o (i_{max} + i_{mid})/2 \\ & + t_n (i_{mid} + i_{min})/2 = i_{oref} T_s. \end{aligned} \tag{6}$$

By combining (4)–(6), the following expressions can be obtained:

$$\begin{aligned} f_{stp} &= \frac{(V_{dc} + v_o)\left[(2m+2)\, V_{dc} - \left(m^2 + 2m + 2\right) v_o\right]}{2L_1 V_{dc} (m+2)^2 \,(I_a + i_{oref})} \\ i_{max} &= \\ & \frac{\left[(2m{+}4)\, V_{dc} - (2m{+}4)\, v_o\right] i_{oref} + \left[\left(2 - m^2\right) v_o - 2V_{dc}\right] i_{min}}{(2m{+}2)\, V_{dc} - (m^2{+}2m{+}2)\, v_o} \\ i_{mid} &= \\ & 2 i_{oref} + \frac{2m\, (V_{dc}{+}v_o)\, i_{oref} - \left[\left(m^2{+}4m{+}2\right) v_o - 2V_{dc}\right] i_{min}}{(m^2{+}2m{+}2)\, v_o - (2m{+}2)\, V_{dc}}. \end{aligned} \tag{7}$$

When the output voltage $v_o < 0$ and output current $i_{oref} > 0$, as shown in Fig. 5(b), defining $t_o = m{*}t_n$, the expressions of f_{stp}, i_{max} and i_{mid} similar to (7) can be obtained. When $i_{oref} < 0$, f_{stp}, i_{max}, and i_{mid} can be derived directly from symmetry, and will not be calculated in detail here. They are expressed uniformly as follows:

$$f_{stp} = \frac{(V_{dc} + |v_o|)\left[(2m+2)\, V_{dc} - \left(m^2 + 2m + 2\right) |v_o|\right]}{2L_1 V_{dc} (m+2)^2 \,(I_a + |i_{oref}|)}$$

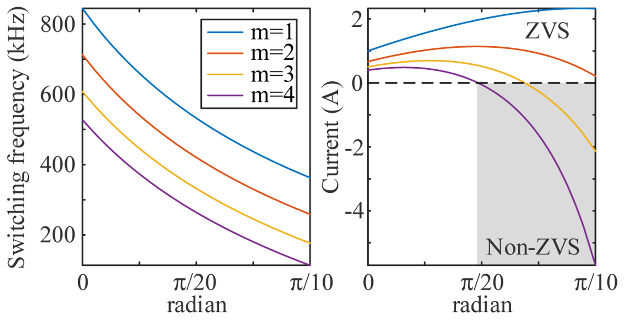

(a) (b)

Fig. 7. Switching frequency and current i_{mid} variation curves with m. (a) Switching frequency curves. (b) Inductor current I_{mid} curves.

$$i_{\max} = \frac{\left[(2m+4)V_{\text{dc}}-(2m+4)|v_{\text{o}}|\right] i_{\text{oref}}+\left[\left(2-m^2\right)|v_{\text{o}}|-2V_{\text{dc}}\right] i_{\min}}{(2m+2)V_{\text{dc}}-\left(m^2+2m+2\right)|v_{\text{o}}|}$$

$$i_{\text{mid}} = 2i_{\text{oref}}+\frac{2m\left(V_{\text{dc}}+|v_{\text{o}}|\right) i_{\text{oref}}-\left[\left(m^2+4m+2\right)|v_{\text{o}}|-2V_{\text{dc}}\right] i_{\min}}{\left(m^2+2m+2\right)|v_{\text{o}}|-(2m+2)V_{\text{dc}}}. \tag{8}$$

Comparing the expressions for f_{su}, f_{sb}, and f_{stp}, it is found that the switching frequency of the QTCM modulation can be changed by adjusting ratio m when the circuit parameters and operating condition are certain.

The curves of f_{stp} and i_{mid} in the interval [0,π/10] for different m are plotted in Fig. 7. As m increases, the frequency near the ac current ZCP decreases significantly, but i_{mid} will be less than zero in some intervals during which ZVS can not be achieved. To realize ZVS, the following constraints need to be satisfied when output current i_{oref} greater than zero:

$$i_{\text{mid}} \geq I_{\text{th}} > \frac{2V_{\text{dc}}C_{\text{oss}}}{t_{\text{d}}} \tag{9}$$

where C_{oss} represents output capacitance and t_{d} is the dead time. I_{th} is taken as 0.8 A to achieve ZVS. If a fixed ratio m is taken during the line cycle, the effect of switching frequency reduction near the ZCP will be limited because a small m needs to be taken. According to Fig. 7, if a large m is taken near the ZCP and the value of m varies with the ac output current, a better frequency reduction effect can be achieved while ensuring that the constraint of i_{mid} is satisfied. Optimization for time-varying m is described below.

III. CO-OPTIMIZATION STRATEGY OF INDUCTOR CURRENT RMS AND SWITCHING FREQUENCY

A. Loss Distribution Analysis

The losses of the single-phase full-bridge inverter shown in Fig. 1 mainly include power devices losses and passive component losses. When the full range ZVS can be achieved, the turn-ON loss and the reverse recovery loss of the diode can be neglected. Thus, power device losses include conduction loss, turn-OFF loss, diode forward conduction loss, and driving loss. The line-cycle averaged conduction loss P_{con} can be calculated as follows:

$$P_{\text{con}} = 2{I_{\text{rms}}}^2 R_{\text{dson}} \tag{10}$$

where I_{rms} is the inductor current rms over a line cycle and R_{dson} can be obtained through Datasheet. For the quasi-trapezoidal inductor current shown in Fig. 5, the rms value is calculated as follows:

$$I_{\text{crms}}^2(t) = \frac{1}{T_{\text{s}}(t)}\left[\begin{array}{l}\int_0^{t_{\text{p}}}\left(i_{\min}(t)+\frac{i_{\max}(t)-i_{\min}(t)}{t_{\text{p}}}t\right)^2 dt\\ +\int_{t_{\text{p}}}^{t_{\text{p}}+t_{\text{o}}}\left(i_{\max}+\frac{(i_{\text{mid}}(t)-i_{\max}(t))(t-t_{\text{p}})}{t_{\text{o}}}\right)^2 dt\\ +\int_{t_{\text{p}}+t_{\text{o}}}^{t_{\text{p}}+t_{\text{o}}+t_{\text{n}}}\left(i_{\text{mid}}(t)+\frac{(i_{\min}(t)-i_{\text{mid}}(t))(t-t_{\text{p}}-t_{\text{o}})}{t_{\text{n}}}\right)^2 dt\end{array}\right]$$

$$I_{\text{rms}} = \frac{2}{T_{\text{g}}}\left(\sum_{k=1}^{f_c/2} I_{\text{crms}}\left(\frac{k}{f_{\text{c}}}\right)\text{round}\left(\frac{T_{\text{c}}}{T_{\text{s}}(k/f_{\text{c}})}\right)\right) \tag{11}$$

where I_{crms} is the inductor current rms during one switching cycle, T_{g} is the line period. T_{c} and f_{c} are control period and control frequency, respectively.

The turn-OFF loss of a GAN HFET is related to its voltage and current during turn-OFF. The switching energy during one turn-OFF period can be given as

$$E_{\text{VIoff}} = \frac{V_{ds}I_d(t)\left(Q_{\text{gd}}+Q_{\text{gs}}\right)\left(R_{gint}+R_{\text{goff}}\right)}{2(|V_{\text{goff}}|+V_{\text{gsth}})} \tag{12}$$

where $I_{\text{d}}(t)$ is the inductor current at turn-OFF, V_{ds} is the drain-source voltage after turn-OFF, V_{gsOFF} is the drive voltage at turn OFF, V_{gsth} is the threshold voltage, R_{gint} and R_{gOFF} are the internal drive resistance and the external turn-OFF resistance, respectively. Q_{gd} and Q_{gs} can be obtained through datasheet [31]. According to Fig. 5, during one switching cycle for QTCM, $I_{\text{d}}(t)$ can be calculated as

$$I_{\text{d}}(t) = i_{\max}(t) + i_{\text{mid}}(t) + 2\left|i_{\min}(t)\right|. \tag{13}$$

Similar with the calculation of I_{rms}, the line cycle averaged turn-OFF loss P_{OFF} is calculated through

$$P_{\text{off}} = \frac{2}{T_{\text{g}}}\left(\sum_{k=1}^{f_c/2} E_{\text{VIoff}}\left(\frac{k}{f_{\text{c}}}\right)\text{round}\left(\frac{T_{\text{c}}}{T_{\text{s}}(k/f_{\text{c}})}\right)\right). \tag{14}$$

The inductor current is renewed by the body diode of GaN during the dead time. If the time of rise and fall of V_{ds} voltage is neglected, the line cycle averaged diode conduction loss P_{vf} during the dead time can be approximated as

$$E_{\text{vf}}(t) = V_{\text{sd}}\left(i_{\max}(t) + i_{\text{mid}}(t) + 2\left|i_{\min}(t)\right|\right) t_{\text{dead}}$$

$$P_{\text{vf}} = \frac{2}{T_{\text{g}}}\left(\sum_{k=1}^{f_c/2} E_{\text{vf}}\left(\frac{k}{f_{\text{c}}}\right)\text{round}\left(\frac{T_{\text{c}}}{T_{\text{s}}(k/f_{\text{c}})}\right)\right) \tag{15}$$

where V_{sd} denotes the body diode conduction voltage drop and E_{vf} denotes the energy lost during one switching cycle. The

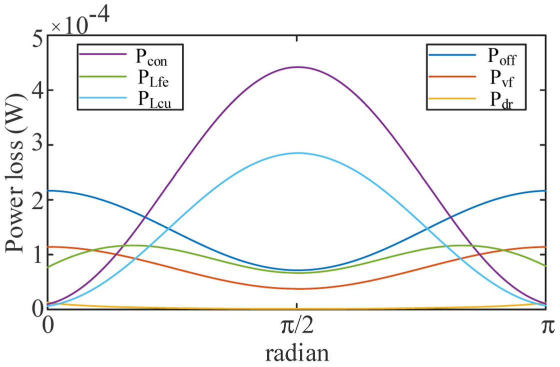

Fig. 8. Distribution of power losses for m = 0 at full load.

driving loss P_{dr} is calculated as follows:

$$P_{\mathrm{dr}} = \frac{2}{T_{\mathrm{g}}}\left(\sum_{k=1}^{f_c/2} Q_{\mathrm{g}} \cdot V_{\mathrm{gs}} \cdot \mathrm{round}\left(\frac{T_{\mathrm{c}}}{T_{\mathrm{s}}\left(k/f_{\mathrm{c}}\right)}\right)\right) \tag{16}$$

where Q_{g} denotes the total gate charge and V_{gs} is the difference between positive and negative drive voltages.

The passive components in this article mainly consider high frequency inductor, whose losses mainly include winding loss and core loss. Winding loss can be calculated as

$$P_{\mathrm{Lcu}} = {I_{\mathrm{rms}}}^2 \cdot R_{\mathrm{L,dc}} + \sum_f R_{\mathrm{L},ac(f)} I_{L(f)}^2 \tag{17}$$

where $R_{\mathrm{L,dc}}$ and $R_{\mathrm{L,ac}}$ are the dc resistance and frequency-dependent ac resistance of the inductor, respectively.

The improved general Steinmetz equation [32] is used to calculated the core loss during each switching cycle

$$\begin{aligned} P_{\mathrm{Lfe}} &= \frac{V_{\mathrm{e}}}{T_{\mathrm{s}}}\int_0^{T_{\mathrm{s}}} k_i \left|\frac{dB}{dT}\right|^{\alpha} (\Delta B)^{\beta-\alpha} dt \\ k_i &= \frac{k}{(2\pi)^{\alpha-1}\int_0^{2\pi} |\cos\theta|^{\alpha} 2^{\beta-\alpha} d\theta} \end{aligned} \tag{18}$$

where k, α, and β can be derived from the Steinmetz parameters of the core material, ΔB is the peak-to-peak flux density in the core in the switching period, and V_{e} is the effective volume of the core.

Fig. 8 shows the losses in each part of the inverter during each control cycle for m = 0 at full load, which is equivalent to TCM. The losses related to the switching frequency account for a high percentage of the total losses in one control cycle near the ZCP. As the inductor current increases and the switching frequency decreases, the conduction loss increases rapidly and becomes the main part of the system losses.

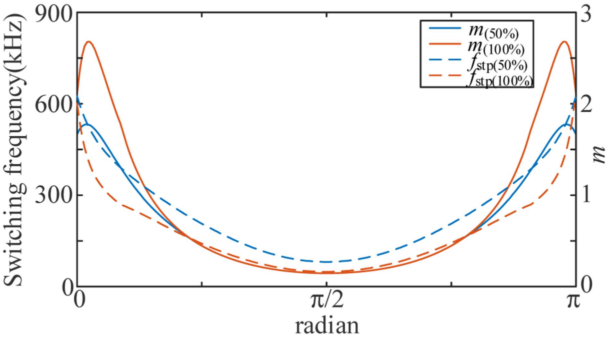

Fig. 9. Optimized *m* and switching frequency curves.

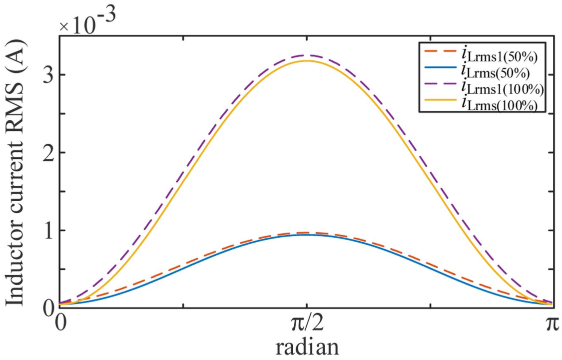

Fig. 10. Inductor current rms of the proposed QCTM and TCM under different operating conditions.

B. Optimization Algorithm

According to the previous analysis, *m* affects the maximum value of the inductor current in each switching cycle and, thus, the inductor current rms in the line cycle. When the load current is large, the conduction loss accounts for a higher percentage of the total loss. When the average value of the inductor current is certain, the inductor current rms during one control cycle can be reduced by optimizing the ratio of zero level *m* during the switching cycle.

The detailed expression of (11) is so complex that it is difficult to directly calculate the optimal *m* to minimize I_{rms}. However, it can be transformed into an optimization problem under certain constraints

$$\begin{aligned} &\min \ I_{\mathrm{rms}}^2 \\ &\mathrm{s.t.} \ \ i_{\mathrm{mid}}. \end{aligned} \tag{19}$$

For (19), *m* can be solved offline by MATLAB. The time-varying *m* and switching frequency determined from (19) are shown in Fig. 9 for 100% load and 50% load. It can be seen that the switching frequency near the ZCP is significantly reduced compared with TCM. At the same time, the switching frequency is continuously varied during the line cycle, avoiding the effect of sudden frequency change on the quality of output current.

The rms and maximum values of the inductor current of QTCM calculated based on the optimized *m* are shown in Figs. 10 and 11, where the solid and dashed lines represent QTCM and TCM, respectively.

According to Fig. 10, it can be seen that the inductor current rms of QTCM is less than that of TCM in each control cycle. At the same reverse current 2 A, the line-cycle averaged inductor

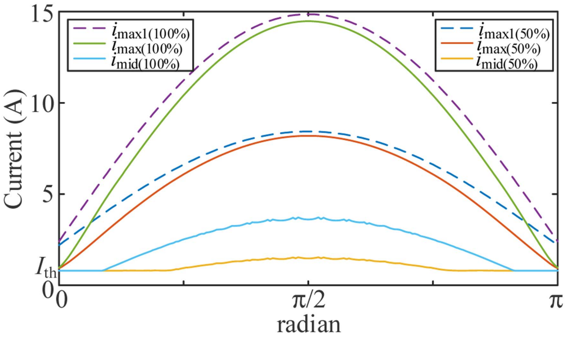

Fig. 11. Peak inductor currents of the proposed QCTM and TCM under different operating conditions.

current rms of QTCM and TCM are 5.68 A and 5.86 A under 100% load, respectively. Rms value of QTCM reduced by 3.07% and conduction loss reduced by 6.06% compared to TCM. When the output power decreases to 50% load, the line-cycle averaged inductor current rms of QTCM and TCM are 3.165 A and 3.309 A. Compared with TCM, there is 4.35% reduction in rms value and 8.51% reduction in conduction loss under QTCM. In Fig. 11, the peak inductor current of QTCM is also smaller than that of TCM in each control cycle. The peak inductor current is reduced by more than 50% around the ZCP, so the associated turn-OFF loss and core loss are also reduced. To achieve the same switching frequency, TCM requires an increase in the reverse current, in which case the proposed QTCM has a greater percentage reduction in the rms and peak values of the inductor current.

According to Fig. 8, for the interval around the ZCP, it is more important to focus on how to optimize m to reduce the losses related to switching frequency. Combined with the principle of QTCM, the larger m is, the smaller f_{stp} is. But at the same time the smaller i_{mid} is. According to Fig. 11, when the inductor current rms is optimal in the interval where the output current is less than I_{a}, i_{mid} is equal to the limiting value, which means that m has reached its maximum value. Thus, frequency optimization and inductor current rms optimization can be achieved simultaneously around the ZCP. For ease of implementation, when output current $i_{\text{oref}} > 0$, fitting an approximation to the i_{mid} in Fig. 11 yields

$$i_{\text{mid}} = \begin{cases} I_{\text{th}}, i_{\text{oref}} \le I_{\text{a}} \\ i_{\text{oref}} + I_{\text{th}} - I_{\text{a}}, i_{\text{oref}} > I_{\text{a}}. \end{cases} \tag{20}$$

Combining (8) and (20), m can be obtained from following equations in real time according to the output voltage and output current:

$$\begin{aligned} & am^2 + bm + c = 0 \\ & a = -I_{\text{a}} v_{\text{o}} - v_{\text{o}} \left(i_{\text{mid}} - 2 i_{\text{oref}} \right) \\ & b = 2 i_{\text{oref}} \left(V_{\text{dc}} + v_{\text{o}} \right) - 4 I_{\text{a}} v_{\text{o}} + \left(2V_{\text{dc}} - 2v_{\text{o}} \right) \left(i_{\text{mid}} - 2 i_{\text{oref}} \right) \\ & c = \left(I_{\text{a}} + i_{\text{mid}} - 2 i_{\text{oref}} \right) \left(2V_{\text{dc}} - 2v_{\text{o}} \right). \end{aligned} \tag{21}$$

The distribution of losses of the inverter calculated based on the optimized time-varying m for the full load and half load is

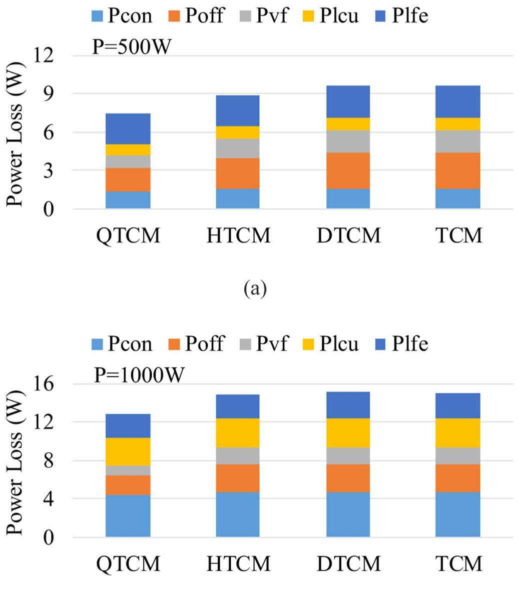

(a)

(b)

Fig. 12. Comparison of main losses of the inverter under different modulation strategies. (a) Under half load (500 W). (b) Under full load (1000 W).

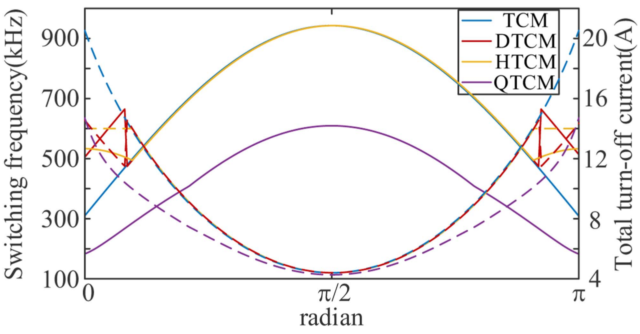

Fig. 13. Switching frequency distribution and total turn-off current during the switching cycle with different modulation strategies under half load (dashed line: switching frequency, solid line: total turn-OFF current).

shown in Fig. 12. Besides, Fig. 12 also represents the theoretical losses of conventional TCM, hybrid TCM [20], dual-zone TCM [30]. In hybrid TCM, the maximum switching frequency of the converter is limited to 600 kHz by changing the reverse current I_{a} in real time. For dual-zone TCM, I_{a} increases to 3 A when the output current phase is less than pi/12, and remains at 2 A at other moments. It can be seen that the total loss of the proposed strategy is significantly smaller than the other three. The switching frequency distribution and total turn-OFF current during the switching cycle with different modulation strategies at 500 W are shown in Fig. 13. Although the switching frequency can be effectively reduced by increasing the reverse current, it is accompanied by an increase in conduction loss. In addition, an increase in reverse current results in an increase in turn-OFF current, so the reduction in turn-OFF loss is limited. According to Figs. 9–11, the proposed QTCM reduces the switching frequency while decreasing the turn-OFF and RMS currents, so that both conduction loss and turn-OFF loss are optimized.

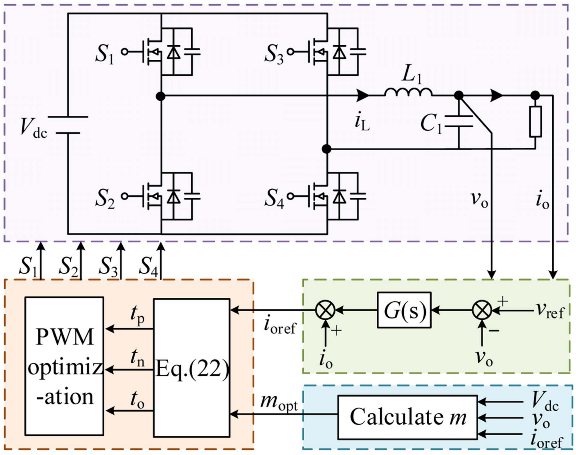

Fig. 14. Block diagram of the proposed control scheme.

IV. CLOSED LOOP CONTROL AND ZERO CROSSING SWITCHING OPTIMIZATION

A. Proposed Control Scheme

The proposed optimal control method of inductor current needs to calculate the ratio m according to the output voltage and current information. Fig. 14 represents the block diagram of the proposed control strategy. i_{oref} is obtained by output voltage closed-loop control and current feed-forward control. Then substituting i_{oref} and v_o into (21), m_{opt} is calculated online by solving the quadratic equation. When the output voltage amplitude is less than 5 V, m is directly given as 1.8 to avoid calculation errors. When the dc bus voltage or load fluctuates, the proposed control strategy can respond quickly and update the value of m in real time. When the output voltage is positive, expressions of t_p, t_o, t_n are shown in (22), and the case where the output voltage is negative can be obtained by symmetry

$$\begin{aligned} t_p &= \frac{L_1(2m+4)(|i_{ref}|+I_a)}{(2m+2)V_{dc}-(m^2+2m+2)v_o} \\ t_o &= mt_p \\ t_n &= \frac{t_p(V_{dc}-v_o-mv_o)}{V_{dc}+v_o}. \end{aligned} \tag{22}$$

B. Proposed Switching Sequence Optimization Method

In the theoretical analysis, for the sake of consistency between the positive and negative half line cycle, the S_1 and S_4 conduction modes are selected as the starting point of the switching cycle during the positive half cycle of the current, and the S_2 and S_3 conduction modes are selected as the end of the switching cycle. Both initial and terminating inductor currents are -I_a. However, during the negative half cycle of the current, both the initial and terminating inductor currents are I_a. Direct switching between positive and negative half cycle will cause the inductor current start point to deviate from the theory, resulting in output current distortion. And ZVS conditions cannot be met when switching directly.

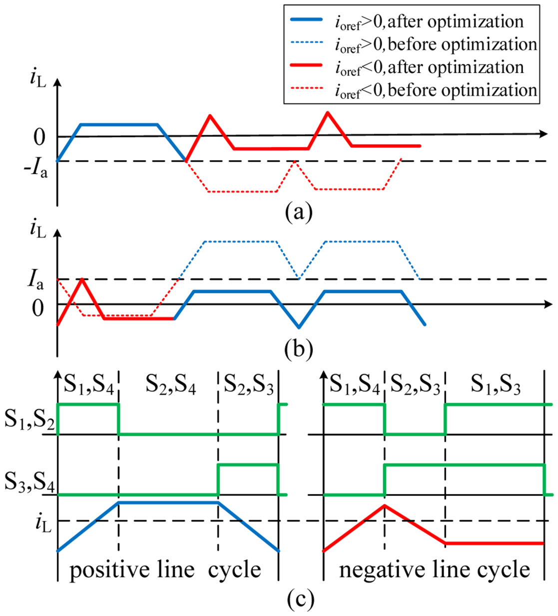

Fig. 15. Optimization of current zero crossing switching. (a) From positive to negative. (b) From negative to positive. (c) Optimized switching sequence.

In order to improve the current quality during the zero crossing switching and to minimize changes to the algorithm structure, an optimized switching sequence is proposed to achieve smooth zero crossing switching, as shown in Fig. 15. The switching sequence in the positive half line cycle remains unchanged. In the negative half cycle, the S_1, S_4 conduction mode is used as the starting point of the switching cycle, followed by the S_2, S_3 conduction mode, and finally the S_1, S_3 conduction mode. The inductor current waveforms during the zero crossing switching before and after optimization are shown in Fig. 15(a) and (b). The difference of 2I_a is compensated through the S_1, S_4 conduction period during which the inductor current increases. At the same time, the ZVS condition during zero crossing switching is satisfied. The proposed method is simple and effective. Smooth switching is realized between positive and negative half line cycles without the need for special transition mode.

V. EXPERIMENT RESULTS

A single-phase full-bridge inverter prototype is built with GaN high-electron-mobility transistors (HEMTs) to verify the proposed adaptive optimal QTCM method, which is shown in Fig. 16. The parameters of the prototype are shown in Table I. The experimental prototype consists of a single-phase full-bridge inverter and a Buck-type power decoupling circuit, which will be used to replace the large dc-link capacitor in the dc bus and not described here. GS0650302L (650 V, 68 mΩ) is selected as power device for the inverter. High-frequency inductor core is made of DMR50 ferrite material from DMEGC. The control scheme of the prototype is implemented based on the DSP TMS320F28377D whose clock frequency is 200 MHz.

The output current waveforms and inductor current waveforms under output power of 1000 W and 500 W are shown in Fig. 17(a) and (b), respectively. The output current is a

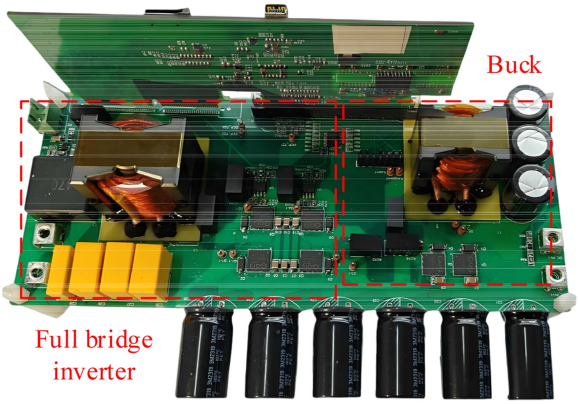

Fig. 16. Laboratory prototype of 1-kW full-bridge inverter.

TABLE I
PARAMETERS OF THE PROTOTYPE

Description	Value
Input voltage V_{dc}	380V
Output voltage v_o	311V(50Hz)
Rated output power P_o	1kW
Output inductor L_1	50μH
Filter capacitance C_1	3μF

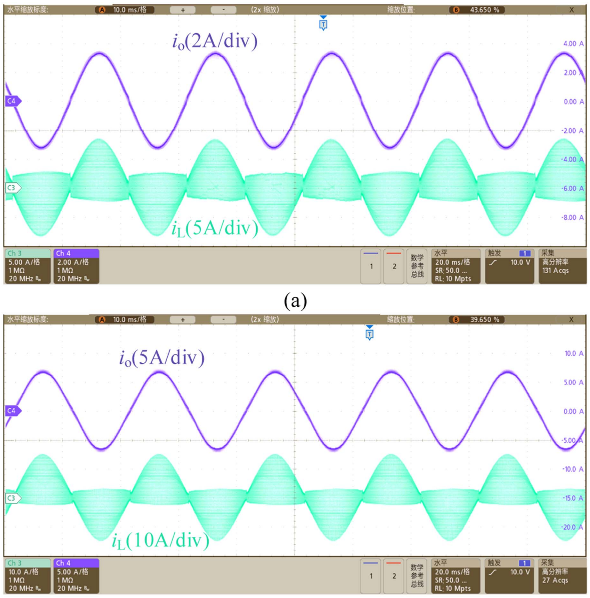

Fig. 17. Output current and inductor current waveforms. (a) Half load. (b) Full load.

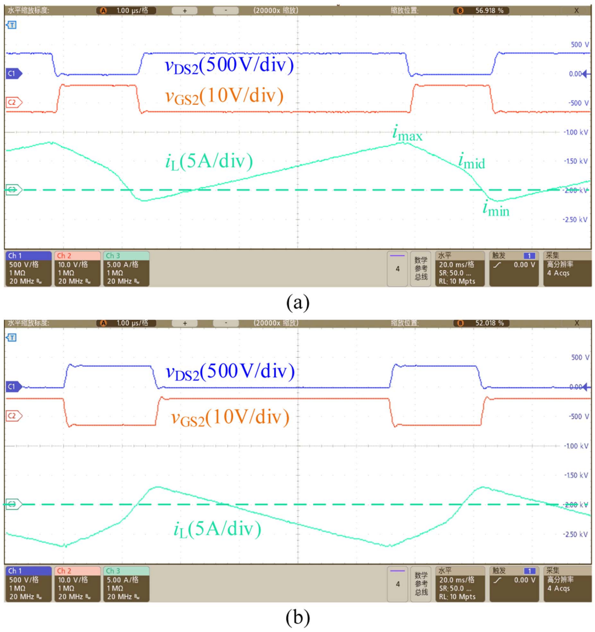

Fig. 18. Detailed switching waveforms. (a) Output current is positive. (b) Output current is negative.

line frequency sine wave, and the inductor current is a high frequency quasi-trapezoidal wave. The input voltage/current and output voltage/current are simultaneously measured by HIOKI power analyzer PW8001, HIOKI current probe CT6841A with a maximum range of 20 A, and the efficiency is directly calculated by the power analyzer. In order to minimize the measurement error, the 1 min average value of the efficiency was used as the measurement value.

The system efficiency is 97.2% (Buck converter is not included) at 500 W output, and the THD of output current is 2.15%. When the output power rises to 1000 W, the system efficiency rises to 98.3%, and the THD of output current is reduced to 1.86%. It indicates that the proposed control scheme has good steady-state performance.

The lower boundary of the inductor current during positive half-cycle and the upper boundary of the inductor current during negative half-cycle in Fig. 17 are not flat due to the sampling error and control delay, which can also be found in [20], [27], and [28]. Both t_p, t_o, and t_n are calculated in real time based on the sampled voltage and current information. Sampling error and control delay lead to errors between the actual control variables and the desired one, so the actual reverse current is not equal to the set value. However, the average value of the inductor current is almost unaffected under closed-loop control, so the THD of the output current can meet the requirement. Even if the reverse current is controlled by a high speed analog comparator, the actual boundary is different from the set value due to the turn OFF delay of the power switches, which has been explained in [25].

The switching cycle waveforms of high-frequency inductor current are shown in Figs. 18 and 19. The DS voltage v_{DS2}, GS voltage of v_{GS2} and inductor current are shown from top to bottom in the figure.

Fig. 18(a) and (b) shows the inductor current waveforms when the output current is positive and the output current is negative, respectively. As shown in Fig. 18(a), when the output current is positive, the current corresponding to the conduction of S_2 is i_{max}. Before the drive signal of S_2 arrives, i_{max} discharges the junction capacitance of S_2, v_{DS2} drops to almost 0, and S_2 achieves ZVS. The ON-time period of S_2 corresponds to the

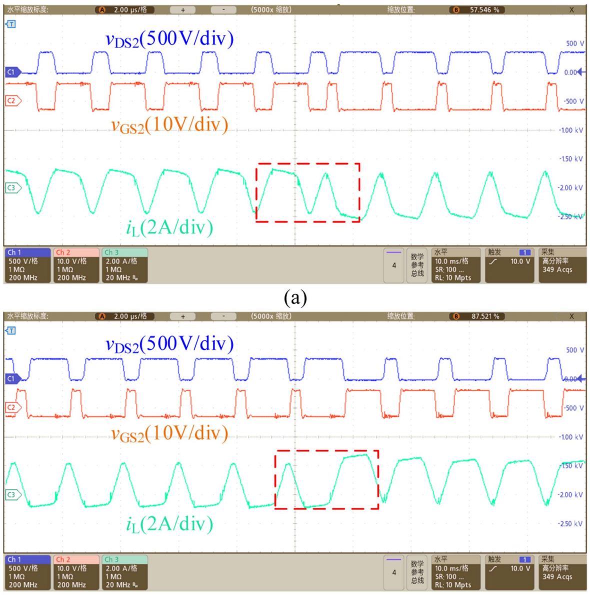

(a)

(b)

Fig. 19. Zero crossing switching cycle waveforms of QTCM. (a) Output current from positive to negative. (b) Output current from negative to positive.

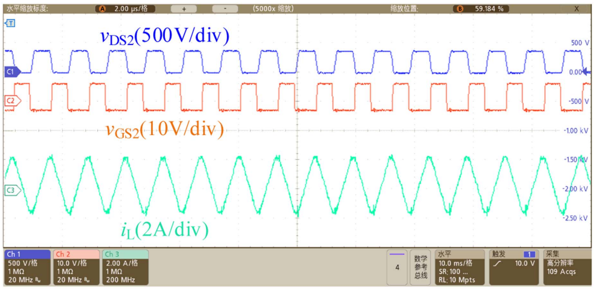

Fig. 20. Switching waveforms near the ZCP of TCM.

stages of Fig. 3(b) outputting zero level and Fig. 3(d) outputting negative level. The voltage across the inductor is negative and the inductor current i_L decreases, the slope of i_L in the zero level stage is less than that in the negative level stage. At the end of the zero level stage the inductor current is i_{mid} greater than 0, satisfying the ZVS condition of S_3. At the moment of S_2 switching OFF, the inductor current is i_{min} less than 0, which satisfies the ZVS condition of S_1 and S_4 in the next stage. As shown in Fig. 18(b), when the output current is negative, the current corresponding to the conduction of S_2 is the reverse current I_a, and ZVS is also achieved. The ON-time period of S_2 corresponds only to the negative level stage in Fig. 3(d), where the inductor current decreases.

Fig. 19(a) and (b) shows the zero crossing switching cycle waveforms for output current from positive to negative and from negative to positive, respectively. Unlike Fig. 18, the zero level stage near the ZCP accounts for a large portion of the switching cycle, which causes the switching frequency to be drastically reduced. As shown in Fig. 19(a), the current corresponding to the conduction of S_2 is less than the reverse current I_a, which means that the peak inductor current of the proposed QTCM decreases during the switching cycle. In the zero level stage the voltage across the inductor is small, which results a low rate of change of inductor current. So, the currents corresponding to S_2 ON and OFF moments are almost the same. Soft switching of S_2 and S_3 is achieved due to the same ZVS condition. When the output current changes from positive to negative, the inverter first outputs a positive level to make the inductor current increase to greater than 0, which compensates for the difference formed by the different reverse currents in the positive and negative half line cycle, and at the same time the ZVS condition is satisfied. Smooth switching of current zero crossing is realized by the proposed switching sequence optimization method. Comparing Figs. 18 and 19, the proposed strategy adaptively selects different ratio m to ensure ZVS is achieved while reducing the inductor current rms at different stages of the output current.

Fig. 20 shows the switching cycle waveforms near the ZCP of TCM. Comparing Figs. 19 and 20, it can be calculated that the peak switching frequency of the proposed QTCM is reduced by about 32%. In order to achieve the same switching frequency reduction, the reverse current near the ZCP needs to be increased by approximately 43% for either constant or variable reverse current control, which is used in [20], [28], [29], and [30]. The experimental results of hybrid TCM and dual zone are shown in Fig. 21. The maximum switching frequency is limited to 600 kHz by increasing the reverse current. It can be seen that the reverse current near the ZCP increases significantly compared with Fig. 17. As shown in Fig. 21(c), the reverse current near the ZCP of hybrid TCM is about 2.8 A. Comparing Figs. 19–21, when the switching frequency is reduced by increasing the reverse current, both the turn-OFF current and the inductor current rms increase compared with the proposed strategy. Therefore the conduction loss will increase.

If the DCM is used, it is necessary to accurately monitor the zero crossing point of the high-frequency inductor current during each switching cycle and precisely control the dead time, which increases the hardware cost. Besides, DCM mode has extra partial hard-switching losses compared with TCM.

The experimental results of the dynamic response of the proposed QTCM are shown in Figs. 22 and 23. As shown in Fig. 22, the output current remains stable when the dc bus voltage drops from 420 V to 340 V and steps from 340 V to 420 V. In Fig. 23, the dynamic response is very fast and smooth when the output power is stepped up from nearly 0 W to 1000 W. And the output voltage remains stable.

Fig. 24 shows the efficiency curves with different modulation strategies. The efficiency of the proposed QTCM outperforms that of hybrid TCM, dual zone TCM, and conventional TCM under different load conditions. When the output power is greater than 600 W, the efficiency of hybrid TCM and dual zone TCM is almost the same as that of TCM, while the proposed strategy is slightly better than that of TCM. The peak efficiency is improved about 0.2%. The overall switching frequency of TCM is higher during the line cycle under light load, and the efficiency improvement of the proposed optimized QTCM is more obvious. When the output power drops to 200 W, the efficiency of the proposed strategy is improved by 0.8% compared with TCM.

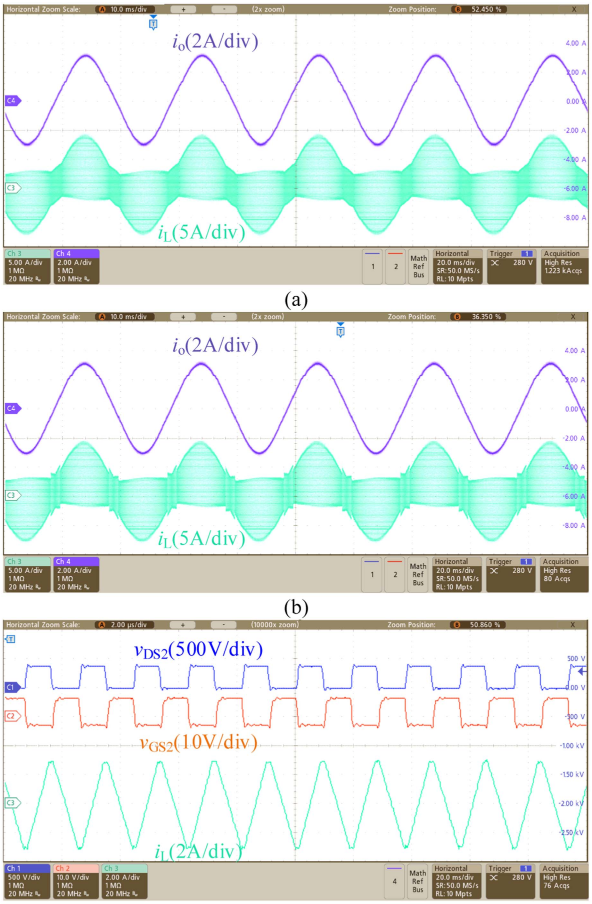

(a)

(b)

(c)

Fig. 21. Output current and inductor current waveforms of hybrid TCM and dual -zone TCM. (a) Hybrid TCM under 500 W. (b) Dual-zone TCM under 500 W. (c) Switching waveforms near the ZCP of hybrid TCM.

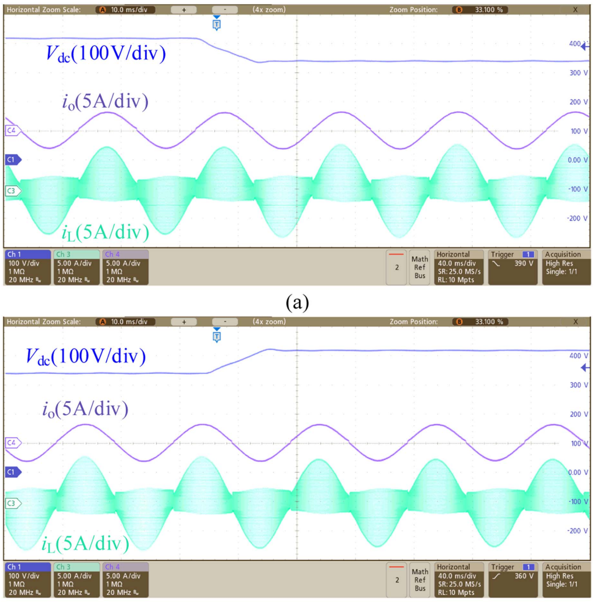

(a)

(b)

Fig. 22. Dynamic experimental results of input voltage variation. (a) DC bus voltage drops from 420 V to 340 V. (b) DC bus voltage steps from 340 V to 420 V.

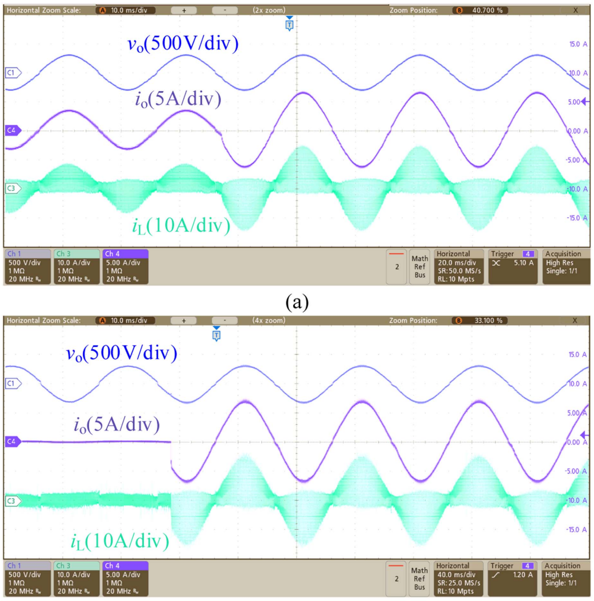

(a)

(b)

Fig. 23. Dynamic experimental results of load transients. (a) 50%–100% load step. (b) 0–100% load step.

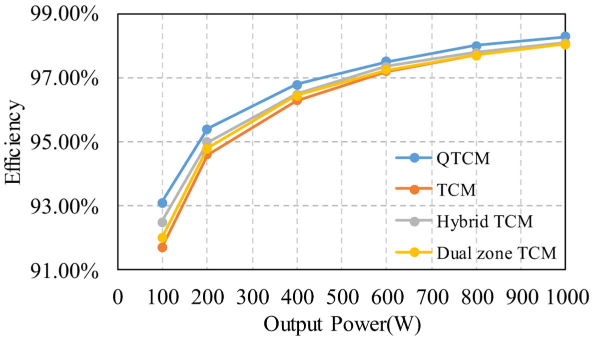

Fig. 24. Measured efficiency comparison with different modulation strategies.

Compared with hybrid TCM and dual zone TCM, the measured efficiency of the proposed strategy is improved by 0.4% and 0.6%, respectively. When the proposed QTCM is applied to higher power levels, parallel of power switches is required to reduce the current stress on the switches. In addition, the combination of QTCM and CCM can be adopted to improve the overall efficiency of the converter.

The comparison of different ZVS methods for the full bridge inverter is shown in Table II. The comparison is made in terms of ZVS range, inductor current rms, rated power, peak efficiency, inductance, and switching frequency. From Table II, it can be seen that the DCM-based method is the most effective in reducing the switching frequency. But it cannot realize full-range soft-switching and requires the addition of a high-precision zero current detection circuit, which is not required in the proposed strategy. Thus, the proposed QTCM lowers the hardware cost and the complexity of control circuits. Compared with the method of varying the reverse current, the proposed strategy

TABLE II
COMPARISON OF DIFFERENT ZVS METHODS

Optimization method	**ZVS range**	**Inductor current RMS**	**Rated power**	**Peak efficiency**	**Inductance**	**Switching frequency**
Multilevel technique[25]	Full	Medium	300W (T-type)	98.7%	300μH	25kHz~ Unknown
HQCCM[23]	Partial ZVS	High	4.4kW (4 leg)	98.55%	170μH	150kHz
Hybrid DCM +TCM[27]	Partial ZVS	Low	500W (2 leg)	98%	150μH	50 kHz ~100kHz
CRM+DCM+ TCM[28]	Partial ZVS	Medium	2.4kW (2 leg)	98.1%	7μH	300kHz ~1MHz
Hybrid TCM[20]	Full	High	1kW (4 leg)	close to 98%	34μH	300kHz ~3MHz
This paper	Full	Lowest	1kW (2 leg)	98.3%	50μH	70kHz ~620kHz

not only reduces the switching frequency but also decreases the inductor current RMS. So, both the turn-OFF loss and conduction loss are optimized.

VI. CONCLUSION

In this article, a switching frequency and inductor current rms co-optimization strategy for single-phase soft-switching inverter is proposed. The proposed strategy adaptively adjusts the ratio of zero level in the switching cycle according to the output voltage and current for switching frequency and efficiency co-optimization. By constructing a quasi-trapezoidal inductor current, the switching frequency range is optimized and the peak switching frequency is reduced by about 32% without increasing the reverse current. Besides, the peak inductor current and the inductor current rms are reduced at the same time, and thus, the system efficiency is improved. A uniform operating mode is adopted throughout the entire line cycle, and there is no mode switching. Smooth switching of the current zero crossing is achieved by optimizing the switching sequence. The effectiveness of the proposed QTCM modulation strategy is experimentally verified with a peak efficiency of 98.3%.

REFERENCES

[1] K. A. Kim, Y.-C. Liu, M.-C. Chen, and H.-J. Chiu, "Opening the box: Survey of high power density inverter techniques from the little box challenge," *CPSS Trans. Power Electron. Appl.*, vol. 2, no. 2, pp. 131–139, 2017.

[2] J. Millán, P. Godignon, X. Perpiñà, A. Pérez-Tomás, and J. Rebollo, "A survey of wide bandgap power semiconductor devices," *IEEE Trans. Power Electron.*, vol. 29, no. 5, pp. 2155–2163, May 2014.

[3] Y. Shen, L. Shillaber, H. Zhao, Y. Jiang, and T. Long, "Desynchronizing paralleled GaN HEMTs to reduce light-load switching loss," *IEEE Trans. Power Electron.*, vol. 35, no. 9, pp. 9151–9170, Sep. 2020.

[4] R. Hou, Y. Shen, H. Zhao, H. Hu, J. Lu, and T. Long, "Power loss characterization and modeling for GaN-based hard-switching half-bridges considering dynamic on-state resistance," *IEEE Trans. Transport. Electrific.*, vol. 6, no. 2, pp. 540–553, Jun. 2020.

[5] Y. Chen and D. Xu, "Review of soft-switching topologies for single-phase photovoltaic inverters," *IEEE Trans. Power Electron.*, vol. 37, no. 2, pp. 1926–1944, Feb. 2022.

[6] Y. Chen et al., "A ZVS grid-connected full-bridge inverter with a novel ZVS SPWM scheme," *IEEE Trans. Power Electron.*, vol. 31, no. 5, pp. 3626–3638, May 2016.

[7] W. Yu, J.-S. Lai, and S.-Y. Park, "An improved zero-voltage switching inverter using two coupled magnetics in one resonant pole," *IEEE Trans. Power Electron.*, vol. 25, no. 4, pp. 952–961, Apr. 2010.

[8] R. Samani, D. S. Beyragh, and M. Pahlevani, "A new grid-connected DC/AC inverter with soft switching and low current ripple," *IEEE Trans. Power Electron.*, vol. 34, no. 5, pp. 4480–4496, May 2019.

[9] F. Liu, J. Wan, L. Jiang, Y. Li, and K.-Z. Liu, "A new soft-switching AC–DC converter based on coupled inductors for onboard charging applications," *IEEE Trans. Power Electron.*, vol. 38, no. 3, pp. 3433–3443, Mar. 2023.

[10] Q. Zhang, H. Hu, D. Zhang, X. Fang, Z. J. Shen, and I. Bartarseh, "A controlled-type ZVS technique without auxiliary components for the low power DC/AC inverter," *IEEE Trans. Power Electron.*, vol. 28, no. 7, pp. 3287–3296, Jul. 2013.

[11] C. Marxgut, F. Krismer, D. Bortis, and J. W. Kolar, "Ultraflat interleaved triangular current mode (TCM) single-phase PFC rectifier," *IEEE Trans. Power Electron.*, vol. 29, no. 2, pp. 873–882, Feb. 2014.

[12] A. Amirahmadi, L. Chen, U. Somani, H. Hu, N. Kutkut, and I. Bartarseh, "High efficiency dual-mode current modulation method for low-power DC/AC inverters," *IEEE Trans. Power Electron.*, vol. 29, no. 6, pp. 2638–2642, Jun. 2014.

[13] S. M. Tayebi and I. Batarseh, "Analysis and optimization of variable-frequency soft-switching peak current mode control techniques for microinverters," *IEEE Trans. Power Electron.*, vol. 33, no. 2, pp. 1644–1653, Feb. 2018.

[14] Y. Levron and R. W. Erickson, "High weighted efficiency in single-phase solar inverters by a variable-frequency peak current controller," *IEEE Trans. Power Electron.*, vol. 31, no. 1, pp. 248–257, Jan. 2016.

[15] Q. Huang and A. Q. Huang, "Variable frequency average current mode control for ZVS symmetrical dual-buck H-bridge All-GaN inverter," *IEEE J. Emerg. Sel. Topics Power Electron.*, vol. 8, no. 4, pp. 4416–4427, Dec. 2020.

[16] H. Yin, T. Lang, X. Li, S. Du, and H. Hu, "A hybrid boundary conduction modulation for a single-phase H-bridge inverter to alleviate zero-crossing distortion and enable reactive power capability," *IEEE Trans. Power Electron.*, vol. 35, no. 8, pp. 8311–8323, Aug. 2020.

[17] D. Shahzad, M. Farooq, S. Pervaiz, and K. K. Afridi, "A high-power-density high-efficiency soft-switched single-phase universal input to 28-V isolated AC–DC converter module designed for paralleled operation," *IEEE Trans. Power Electron.*, vol. 37, no. 7, pp. 8262–8280, Jul. 2022.

[18] K. Sabi and D. Costinett, "Design and implementation of a bipolar-unipolar switched boundary current mode (BCM) control GaN-based single-phase inverter," in *Proc. IEEE Energy Convers. Congr. Expo.*, Baltimore, MD, USA, 2019, pp. 6473–6480.

[19] J. Ning, H. Ben, M. Li, T. Meng, and X. Wang, "High-frequency inverter advanced digital modulation strategy and implementation method considering dead time and switching transient effect," *IEEE J. Emerg. Sel. Topics Power Electron.*, vol. 12, no. 2, pp. 1921–1933, Apr. 2024.

[20] T. Liu, C. Chen, K. Xu, Y. Zhang, and Y. Kang, "GaN-based megahertz single-phase inverter with a hybrid TCM control method for high efficiency and high-power density," *IEEE Trans. Power Electron.*, vol. 36, no. 6, pp. 6797–6813, Jun. 2021.

[21] Z. Zhang et al., "All-fixed switching frequency control of CRM boost PFC converter based on variable inductor in a wide input voltage range," in *Proc. IEEE Energy Convers. Congr. Expo.*, Baltimore, MD, USA, 2019, pp. 1434–1441.

[22] Y. Jiang, Y. Shen, T. Lackie, L. Shillaber, B. Hu, and T. Long, "Realization of adaptive soft-switching in high-frequency single-phase inverter based on parallel half bridges," in *Proc. IEEE Appl. Power Electron. Conf. Expo.*, Houston, TX, USA, 2022, pp. 99–106.

[23] Y. Jiang, Y. Shen, L. Shillaber, B. Hu, C. Jiang, and T. Long, "Hybrid-mode adaptive zero-voltage switching for single-phase DC–AC conversion with paralleled SiC MOSFETs," *IEEE Trans. Power Electron.*, vol. 37, no. 12, pp. 14067–14081, Dec. 2022.

[24] L. Lin, J. Zhang, and S. Shao, "A variable switching frequency multimode control scheme for single-phase grid-tied multilevel PV microinverters," *IEEE Trans. Power Electron.*, vol. 38, no. 9, pp. 11543–11555, Sep. 2023.

[25] Z. Zhang, J. Zhang, S. Shao, and J. Zhang, "A high-efficiency single-phase T-type BCM microinverter," *IEEE Trans. Power Electron.*, vol. 34, no. 1, pp. 984–995, Jan. 2019.

[26] L. Huber, B. T. Irving, and M. M. Jovanovic, "Effect of valley switching and switching-frequency limitation on line-current distortions of DCM/CCM boundary boost PFC converters," *IEEE Trans. Power Electron.*, vol. 24, no. 2, pp. 339–347, Feb. 2009.

[27] Y. Tang, C. Zhang, Y. Guo, H. Sun, and L. Jiang, "Optimization of zero-crossing distortion for unipolar BCM grid-tied inverter," *IEEE J. Emerg. Sel. Topics Power Electron.*, vol. 11, no. 4, pp. 3680–3691, Aug. 2023.

[28] G. Son, Z. Huang, Q. Li, and F. C. Lee, "Analysis and control of critical conduction mode high-frequency single-phase transformerless PV inverter," *IEEE Trans. Power Electron.*, vol. 36, no. 11, pp. 13188–13199, Nov. 2021.

[29] N. Haryani, R. Burgos, and D. Boroyevich, "Variable frequency and constant frequency modulation techniques for GaN based MHz H-bridge PFC," in *Proc. IEEE Appl. Power Electron. Conf. Expo.*, Charlotte, NC, USA, 2015, pp. 1889–1896.

[30] X. Li, Y. Liu, and H. Zhang, "Hybrid-modulation hysteresis scheme based decoupled power control of grid-connected inverter," *IEEE J. Emerg. Sel. Topics Power Electron.*, vol. 11, no. 1, pp. 276–287, Feb. 2023.

[31] R. Hou, J. Xu, and D. Chen, "A multivariable turn-on/turn-off switching loss scaling approach for high-voltage GaN HEMTs in a hard-switching half-bridge configuration," in *Proc. IEEE 5th Workshop Wide Bandgap Power Devices Appl.*, Albuquerque, NM, USA, 2017, pp. 171–176.

[32] I. Villar, U. Viscarret, I. Etxeberria-Otadui, and A. Rufer, "Global loss evaluation methods for nonsinusoidally fed medium-frequency power transformers," *IEEE Trans. Ind. Electron.*, vol. 56, no. 10, pp. 4132–4140, Oct. 2009.

Chaofan Wei received the B.Eng. degree in electrical engineering from Nanjing University of Aeronautics and Astronautics, Nanjing, China, in 2019, and the M.Sc. degree from Southeast University, Nanjing, China, in 2022. He is currently working toward the Ph.D. degree in electrical engineering with the Key Laboratory of Control of Power Transmission and Conversion (Shanghai Jiao Tong University), Ministry of Education, Shanghai, China.

His current research interests include high-efficiency battery energy storage power conversion and grid-connected control technology.

Jianhua Lei was born in Chenzhou, China, in Jul. 1985. He received the B.S. degree in automation from Beihua University, Jilin, China, in 2008, and the M.S. of Engineering degree in materials engineering from Sun Yat-sen University, Guangzhou, China, in 2015. Since 2022, he has been working toward the Ph.D. degree in materials and chemical engineering with Tsinghua University, Shenzhen, China.

His current research interests include power electronic switching power supply control technologies, energy storage inverter technologies, and renewable energy-based water electrolysis for hydrogen production.

Ruogu Yao was born in Chengdu, China. She received the B.S. degree in electrical engineering in 2024 from Shanghai Jiao Tong University, Shanghai, China, where she is currently working toward the M.S. degree in electrical engineering.

Her current research interests include dc–dc converters, dc–ac converters, and soft-switching techniques.

Jiatao Yang received the B.S., M.S., and Ph.D. degrees in electrical engineering from Shanghai Jiao Tong University, Shanghai, China in 2016, 2019, and 2024, respectively.

He is currently a Postdoctoral Researcher with the Key Laboratory of Control of Power Transmission and Conversion (Shanghai Jiao Tong University), Ministry of Education, Shanghai, China. His current research interests include Photovoltaic power generation system, energy storage system, bidirectional dc–dc, and dc–ac converter, as well as renewable energy power conversion.

Rui Li (Senior Member, IEEE) received the Ph.D. degree in electrical engineering from Zhejiang University, Hangzhou, China, in 2010.

From 2008 to 2009, he was an Academic Guest with the Power Electronic Systems Laboratory, Swiss Federal Institute of Technology, Zurich, Switzerland. From 2014 to 2015, he was a Postdoctoral Research Scholar with the Center for Advanced Power Systems, Department of Electrical and Computer Engineering, College of Engineering, Florida State University, Tallahassee, FL, USA. Since 2010, he has been with the Department of Electrical Engineering, School of Electronics, Information and Electrical Engineering, Shanghai Jiao Tong University, Shanghai, China, where he is currently a Professor. His current research interest includes the application of power electronics in renewable energy conversion.

Dr. Li was a recipient of the IEEE Power Electronics Society Transactions Second Prize Paper Award, in 2015.

Wei Yu received the Ph.D. degree in power electronics and power drives from Zhejiang University, Hangzhou, China, in 2009, respectively.

He is currently with the Research and Development Center, EAST Group Company, Ltd., Dongguan, China, as the Chief Technology Officer. His current research interests include new energy applications and power electronics technology, especially in the PV inverter, UPS, power energy storage systems, microgrids, and electric vehicle charging pile.

Shaohui Li received the B.S. degree in electrical engineering from Zhuhai College of Jilin University, Changchun, China, in 2015. He is currently with the R&D Department and Intellectual Property Department, EAST Group Company, Ltd., Dongguan, China, as the IP Director. His current research interests include power electronics technology and intellectual property, especially in the PV inverter, UPS, power energy storage systems, microgrids, and electric vehicle charging pile.